Flexible Dual-structured MXene for Ultra-Sensitive and Ultra-Wide Monitoring of Anatomical and Physiological Movements

Lihao Guo,[1] Zekun Li,[1] Wenwen Hu,[2] Taoping Liu[3], Youbing Zheng,[4] Miaomiao Yuan,[5] Yujie Dai,[1] Ruizhi Ning,[3] Yujin Zhu,[1] Keyu Tao,[1] Min Zhang,[6] Tao Du,[1] Lu Zhang,[1] Chen Su,[1,] Hossam Haick,[4,*] Weiwei Wu[1,*]*

[1] School of Advanced Materials and Nanotechnology, Interdisciplinary Research Center of Smart Sensors, Xidian University, P. R. China

[2] School of Aerospace Science and Technology, Xidian University, P. R. China

[3] Interdisciplinary Research Center of Smart Sensors, Academy of Advanced Interdisciplinary Research, Xidian University, P. R. China

[4] The Department of Chemical Engineering, Technion - Israel Institute of Technology, Israel

[5] The Eighth Affiliated Hospital, Sun Yat-sen University, Shenzhen 518033, China

[6] School of Chemistry and Molecular Engineering, Shanghai Key Laboratory for Urban Ecological Processes and Eco-Restoration, East China Normal University, P. R. China

Corresponding Author: wwwu@xidian.edu.cn; csu@xidian.edu.cn; hhossam@technion.ac.il

Figure S1. The Tyndall effect of MXene nanosheets colloidal aqueous solution.

After ultrasonic intercalating and centrifuging, a homogeneous dark-green colloidal solution is obtained, exhibiting an apparent Tyndall effect (Figure S1). Moreover, the subsequent aqueous solution self-assembly process is facilitated because of the hydrophilia terminated groups on the MXene.

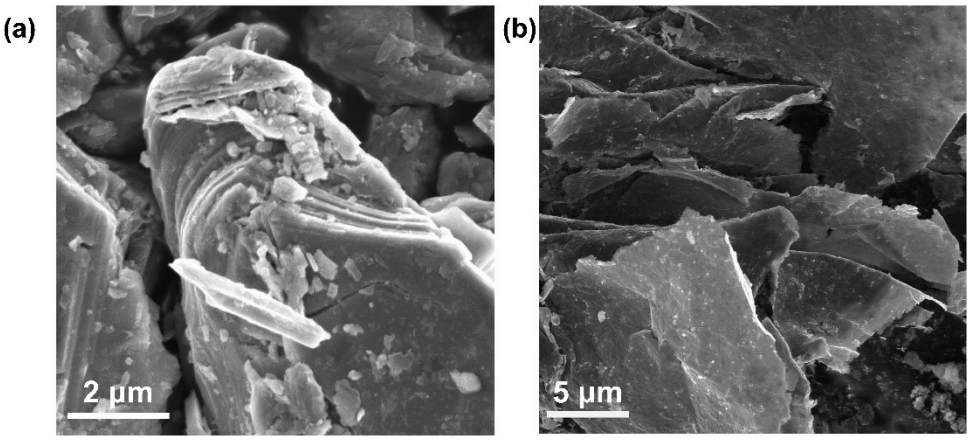

Figure S2. SEM images of (a) Ti_3AlC_2 MAX phase and (b) $Ti_3C_2T_x$ MXene nanosheets.

The SEM images (Figure S2) show that the morphology of MXene nanosheets is significantly different from MAX particles, which transforms from bulk to layered structure. And because of the sample preparation method, the MXene nanosheets aggregate and the actual size of MXene nanosheets is ca. 0.3 μm^2 according to TEM image.

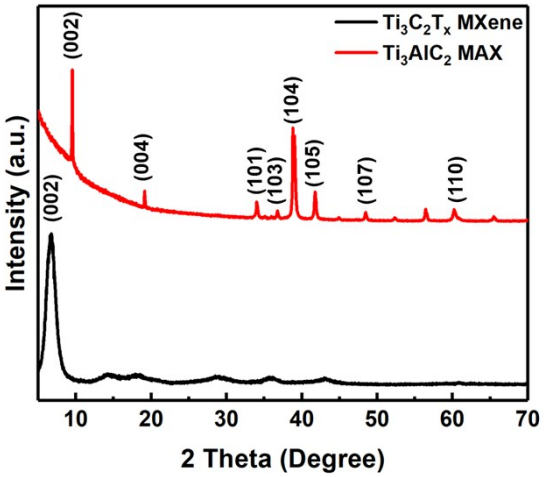

Figure S3. XRD patterns of MAX phase and MXene.

In the X-ray diffraction (XRD) pattern (Figure S3), both the disappearance of the characteristic peak at 39° (indexing to the (104) lattice plane of Ti_3AlC_2 MAX) and the left shift of the peak of (002) from 9.7° to 6.7° (ascribing to a broader interlayer spacing) demonstrate a successful preparation of $Ti_3C_2T_x$ MXene.[1]

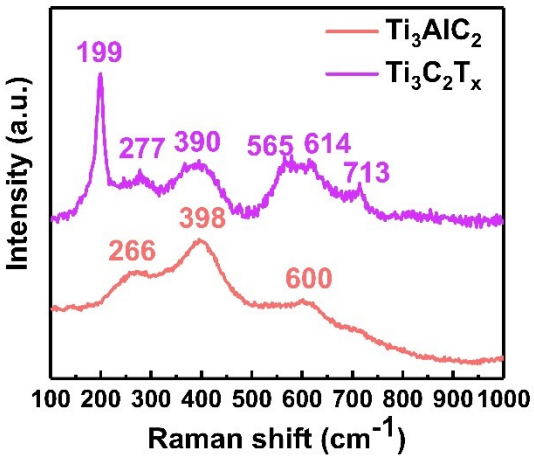

Figure S4. Raman spectrum of Ti_3AlC_2 MAX phase and $Ti_3C_2T_x$ MXene.

According to the Raman fingerprint pattern of $Ti_3C_2T_x$, as shown in Figure S4 (Supporting Information), the peaks at 199 cm^{-1} and 713 cm^{-1} are assigned to out-of-plane vibration modes (A_{1g}), while the peaks between 250 cm^{-1} and 500 cm^{-1} are assigned to in-plane vibration modes (E_g), which has a good agreement with the results reported in the previous work. [2]

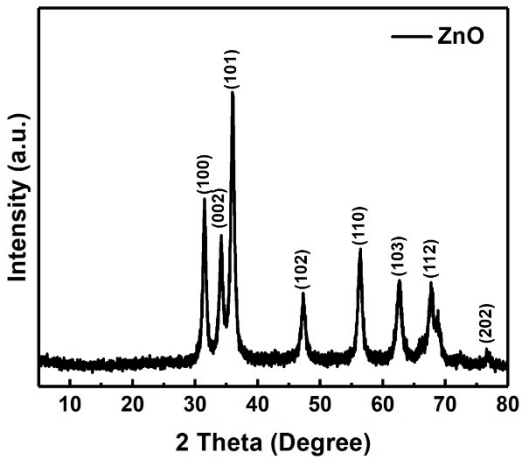

Figure S5. XRD pattern of ZnO spheres.

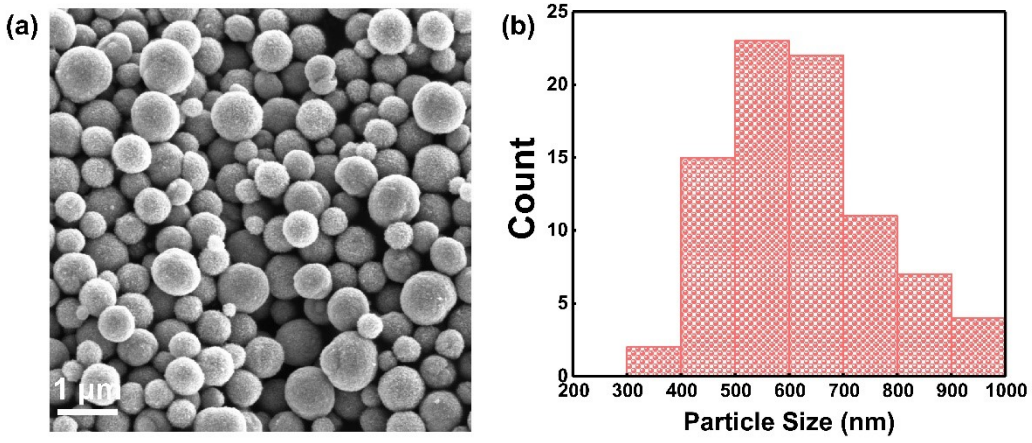

Figure S6. SEM image of (a) ZnO spheres and (b) particle size distribution of ZnO spheres.

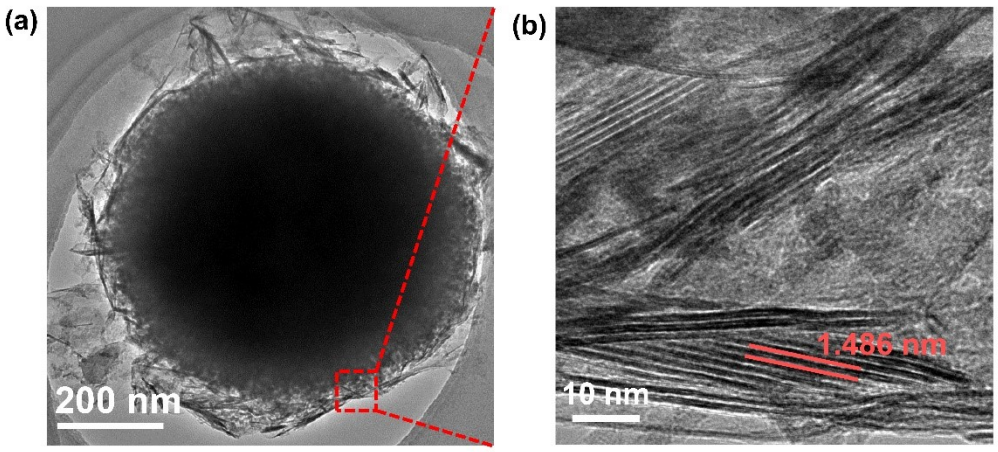

Figure S7. (a) TEM images of ZnO/MXene core-shell composite and HRTEM of part in (a) marked by red block.

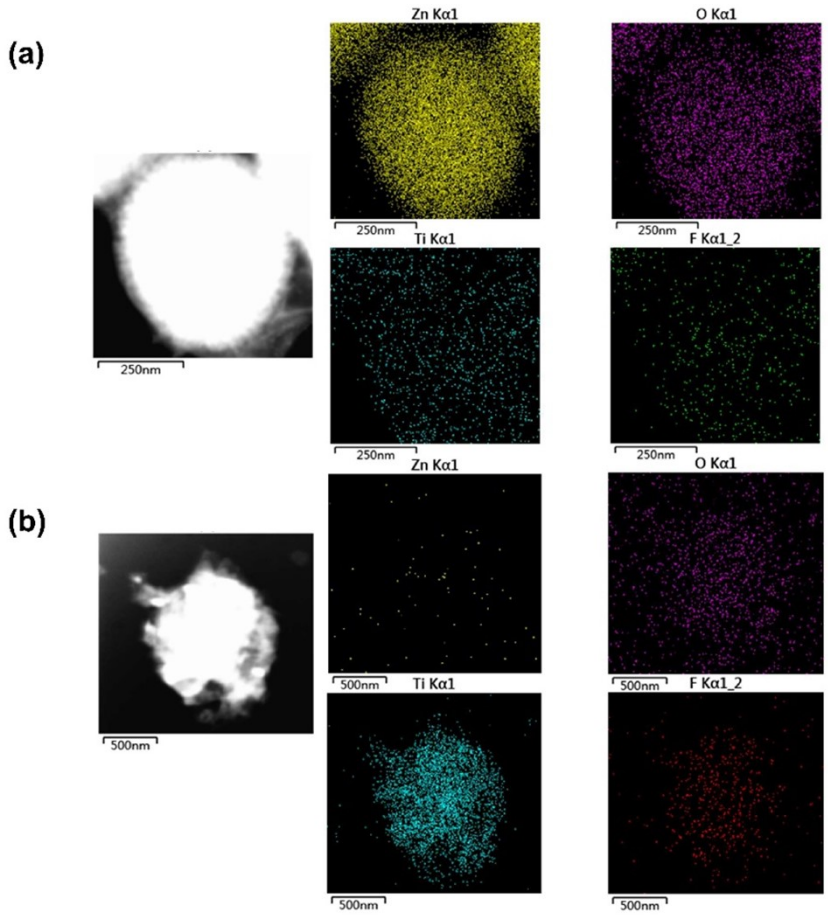

Figure S8. STEM-EDS images of (a) ZnO/MXene core-shell composite and (b) hollow MXene after etching ZnO spheres.

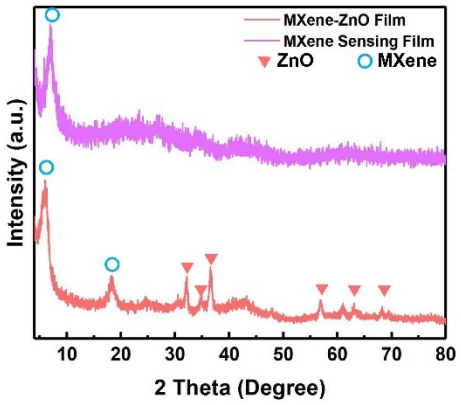

Figure S9. XRD patterns of ZnO-MXene composite film and sensing film after etching ZnO spheres.

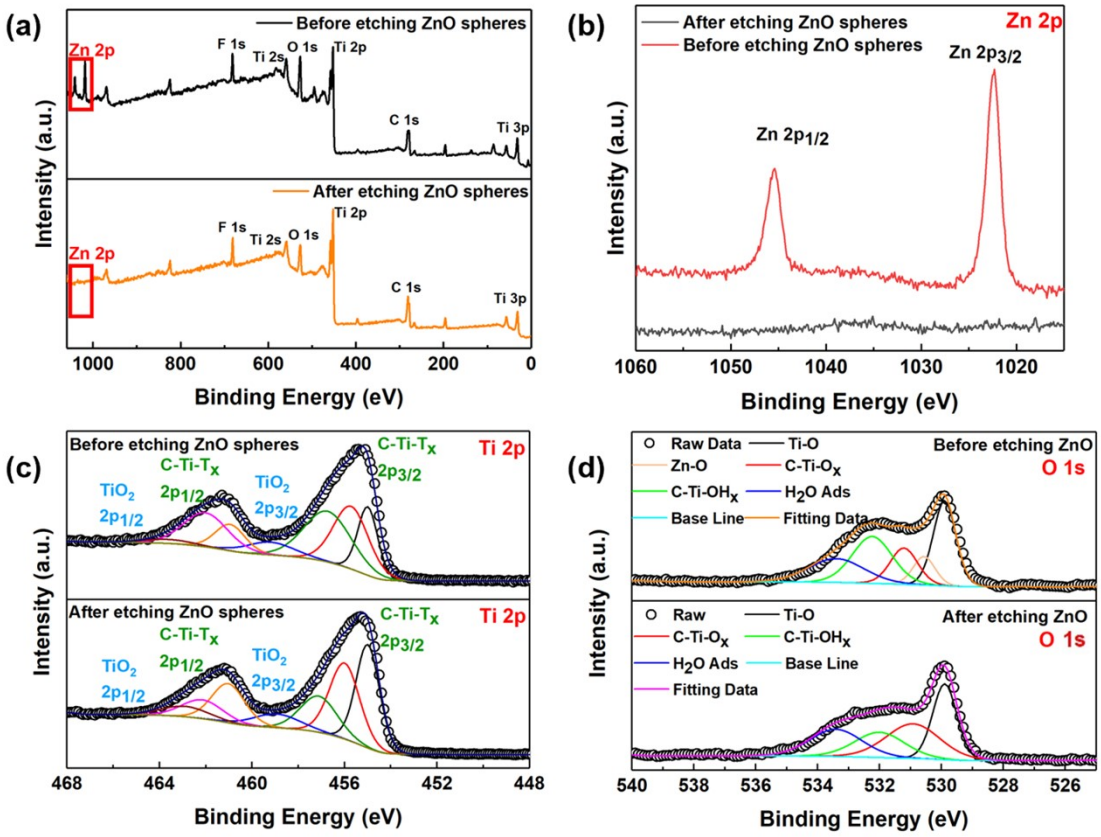

Figure S10. (a) XPS results of sensing film before etching ZnO spheres and after that process, and fine spectrum of (b) Ti 2p, (c) O 1s, and (d) Zn 2p.

The ZnO spheres are the sacrificial templates to build the microstructures for improving the sensors' performance. The XRD pattern of ZnO nanoparticles is shown in Figure S5 in accordance with ZnO standard spectrum (JCPDS NO.36-1451). As

shown in Figure S6a, the size of ZnO spheres is ca. 600 nm (Figure S6b), which is larger than those of MXene nanosheets. Because of the attraction between the negative charge on the surface of MXene and the positive charge on the ZnO, under the action of electrostatic self-assembly, the core-shell ZnO/MXene composite forms when stirring $Ti_3C_2T_x$ MXene nanosheets with ZnO spheres. Due to the different size between ZnO spheres and MXene nanosheets, the smaller MXene nanosheets tended to wrap on the surface of ZnO spheres, and the thickness of the single layer is 1.486 nm (Figure S7), which is similar to reported in the literature.[3] Furthermore, the experiment data of EDS, XRD, and XPS (Figure S8~S10) not only prove the self-assemble process of MXene and ZnO, but also confirm that after immersing in 3M HCl, the MXene isn't oxidized, and there is no residual ZnO spheres. To be specific, the STEM-EDS images (Figure S8) show that the amount of Zn element evidently decrease after etching ZnO spheres while the element of MXene still exist. The XRD pattern can further verify this point in which the diffraction peaks of ZnO disappear and the MXene's diffraction peaks still exist without any oxidation (Figure S9). In high-resolution spectra of Ti 2p, the peaks at 455.2 eV and 461.2 eV corresponding to binding energy of Ti-C are C-Ti-T_x bond of MXene and the peaks at 459.2 eV and 465.3 eV are Ti-O bond of TiO_2.[4] In addition, the high-resolution spectra of O 1s at 529.9 eV and Zn 2p at 1022.33 eV ($2p_{2/3}$) and 1045.49 eV ($2p_{1/2}$) also match well with previously works.[5] [6] The disappearing Zn 2p peaks prove the completely etching of ZnO spheres meanwhile the unchanged spectra of Ti 2p and O 1s show that the oxidation of MXene is negligible.

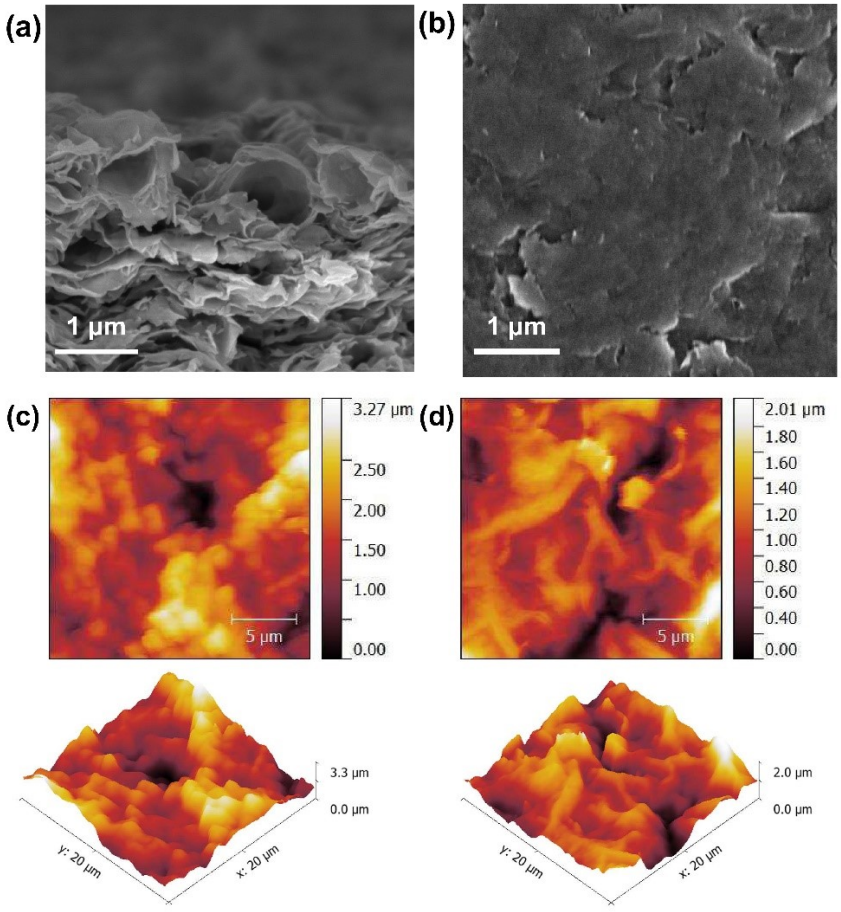

Sample	Ra (nm)	Rq (nm)
Dual-microstructures MXene sensing film	436.309	546.851
Pristine-MXene film	253.858	321.943

Figure S11. SEM images of (a) cross-section of vertical-standing pores and (b) top view of pure MXene film. 2D and 3D AFM images of (c) dual-microstructures MXene sensing film and (d) pristine MXene film and their roughness information.

After dissolving the ZnO sacrificial template, the MXene nanosheets form many vertical-standing pores and wrinkles (Figure S11a) and the surface of pure MXene sensing layer without ZnO sacrificial template is smooth (Figure S11b). The roughness information shown by AFM images can further prove this point.

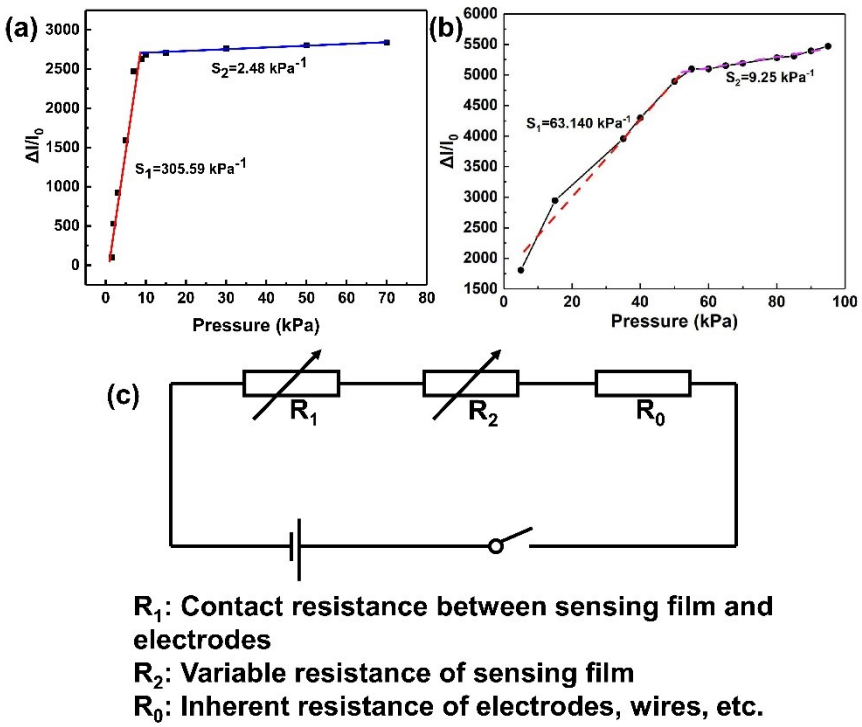

Figure S12. (a) Sensitivity of pristine MXene pressure sensor, (b) sensitivity of two electrodes sensor, and (c) equivalent circuit of dual-microstructures MXene sensor.

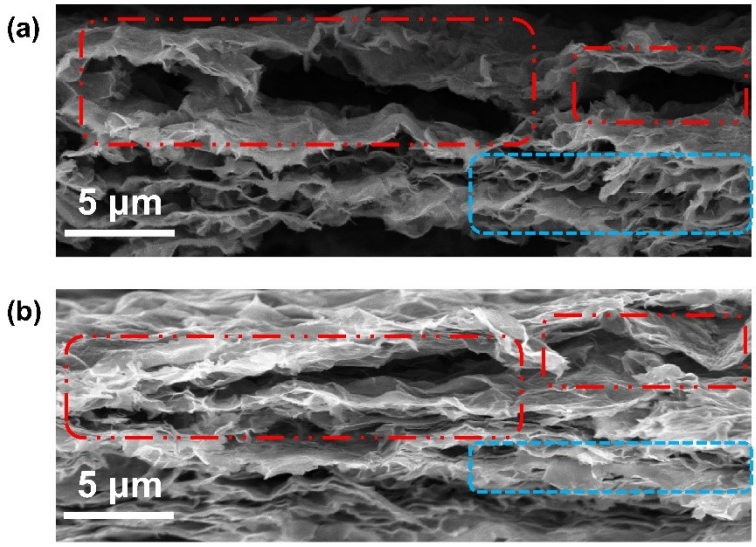

Figure S13. Cross-section SEM images of sensing film in (a) initial state, and (b) under a pressure.

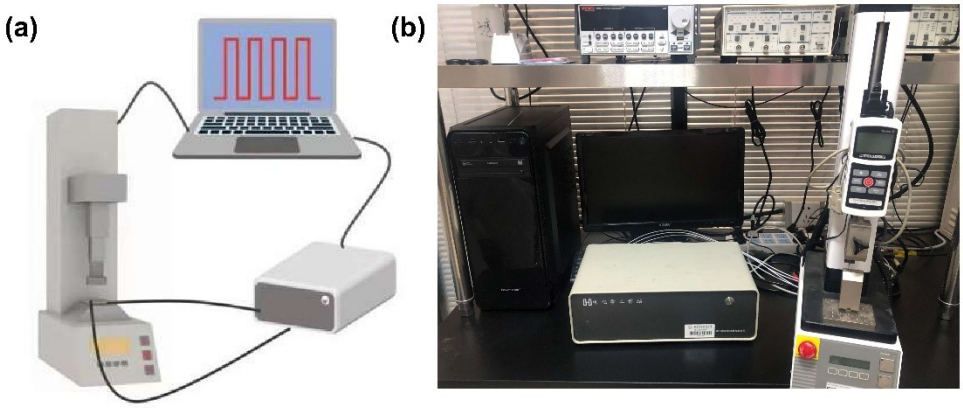

Figure S14. The schematic diagram and photograph of the test system.

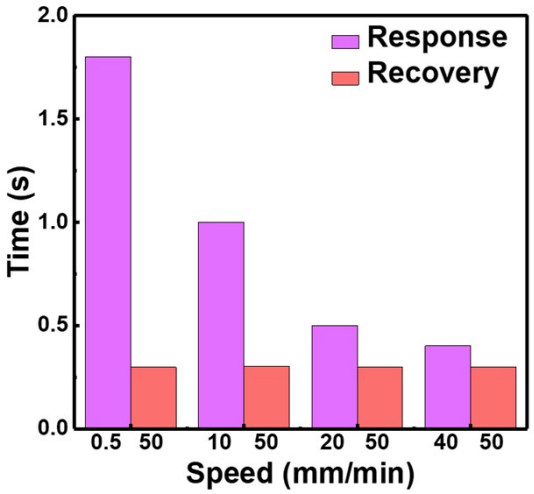

Figure S15. Response and recovery time of sensor with different pressure applied speed.

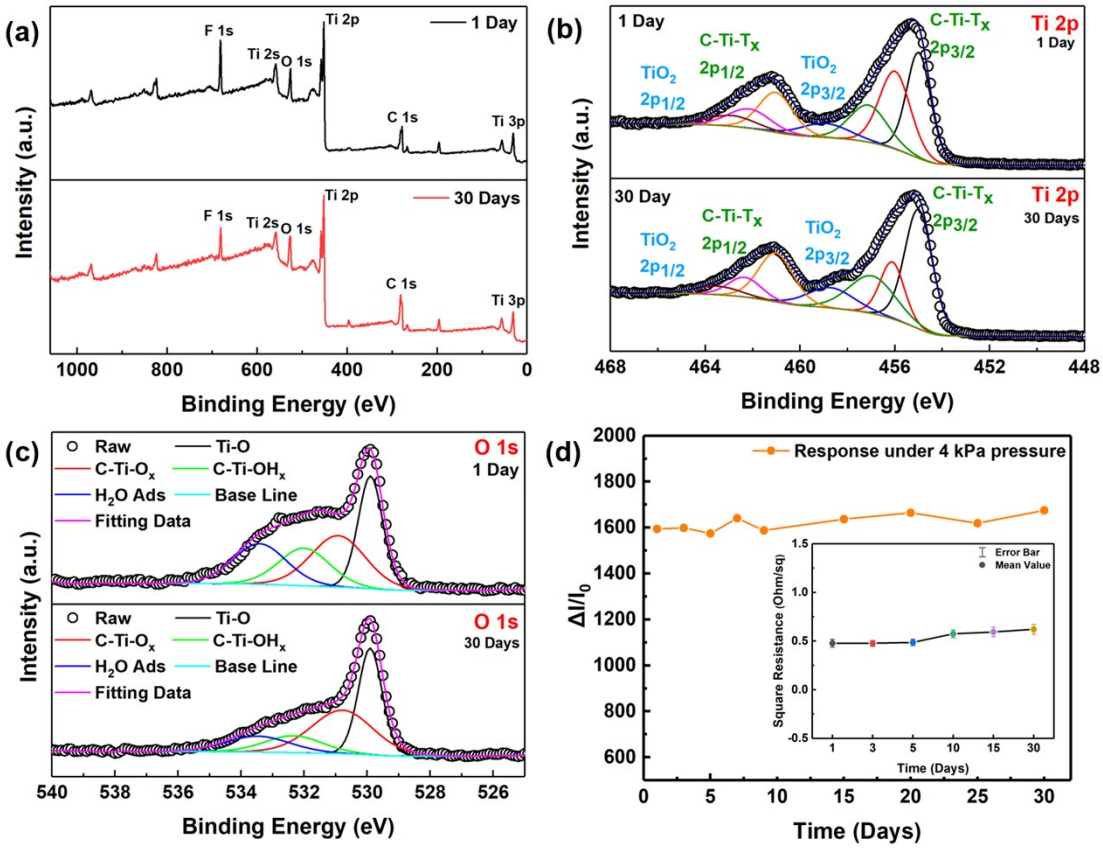

Figure S16. (a) XPS results of sensing film storing for 1 day and 30 days, and fine spectrums of (b) Ti 2p, (c) O 1s. (d) The performance stability test of sensor storing for 1, 3, 5, 7, 10, 15, and 30 days (insert is square resistance of sensing film storing different days tested by Four print probe).

Figure S17. The photograph of gesture recognition device.

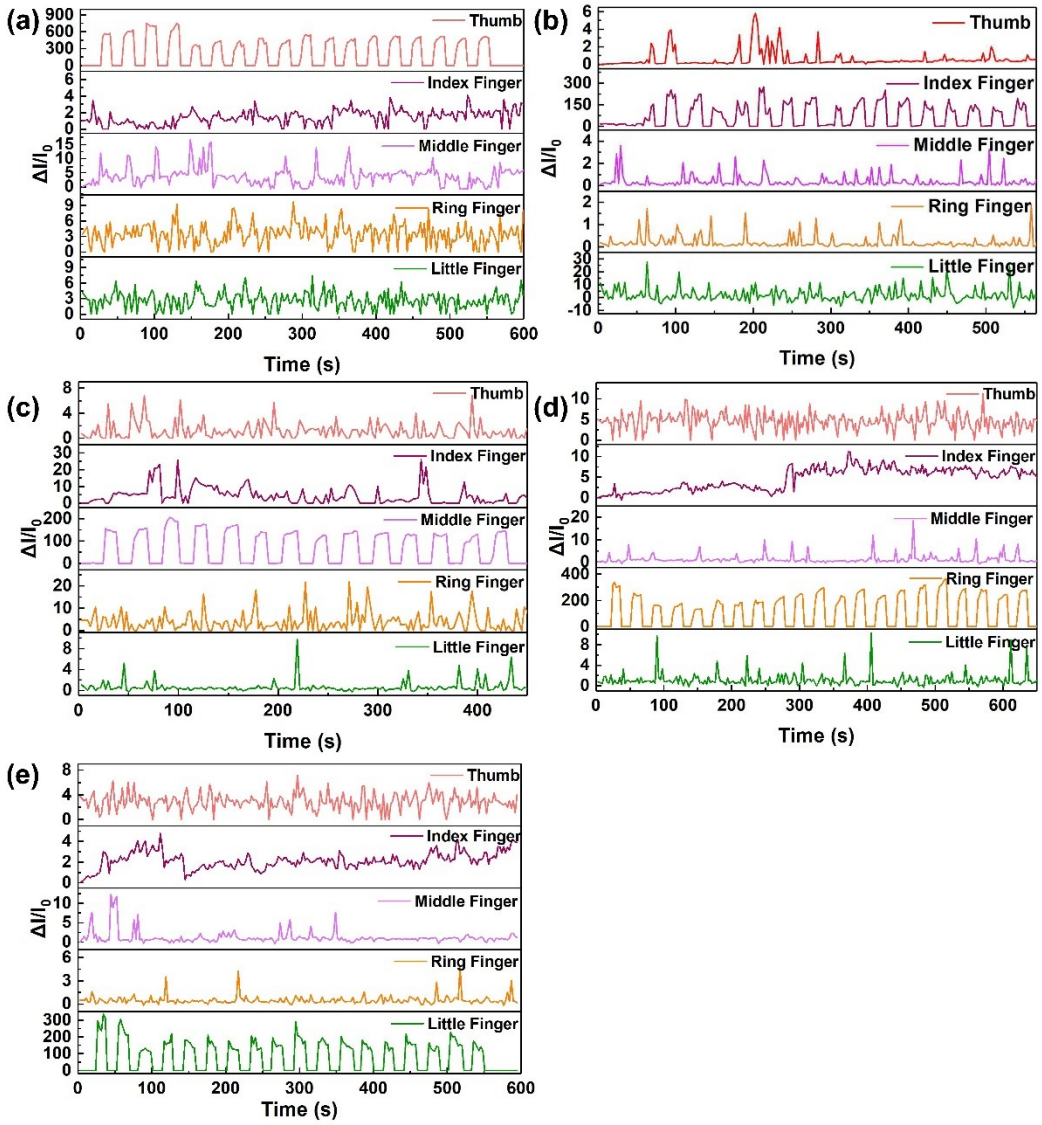

Figure S18. The current signals of five single gestures, (a) thumb bending, (b) index finger bending, (c) middle finger bending, (d) ring finger bending and (e) little finger bending.

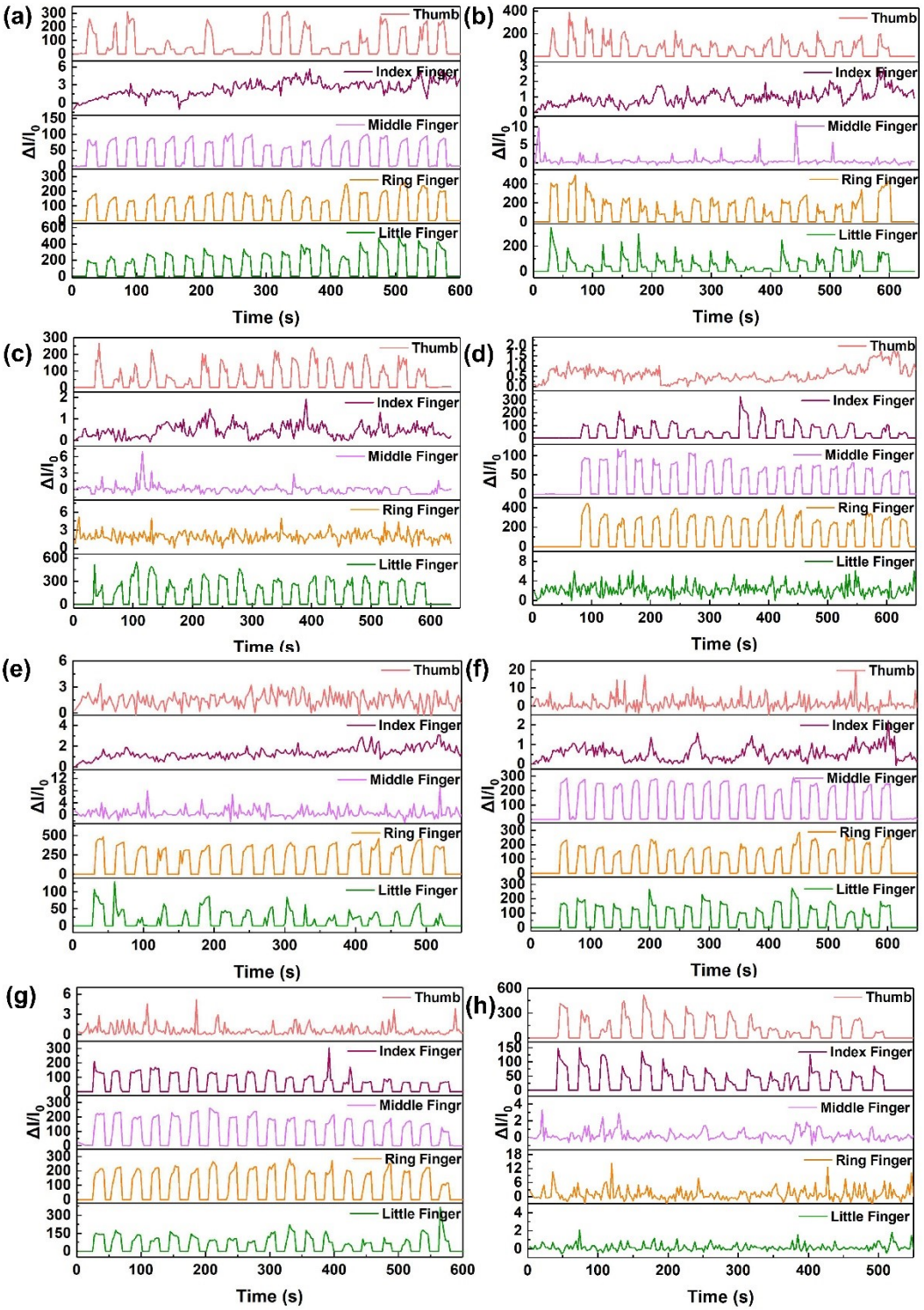
(a)
(b)
(c)
(d)
(e)
(f)
(g)
(h)
Thumb
Index Finger
Middle Finger
Ring Finger
Little Finger
ΔI/I0
Time (s)

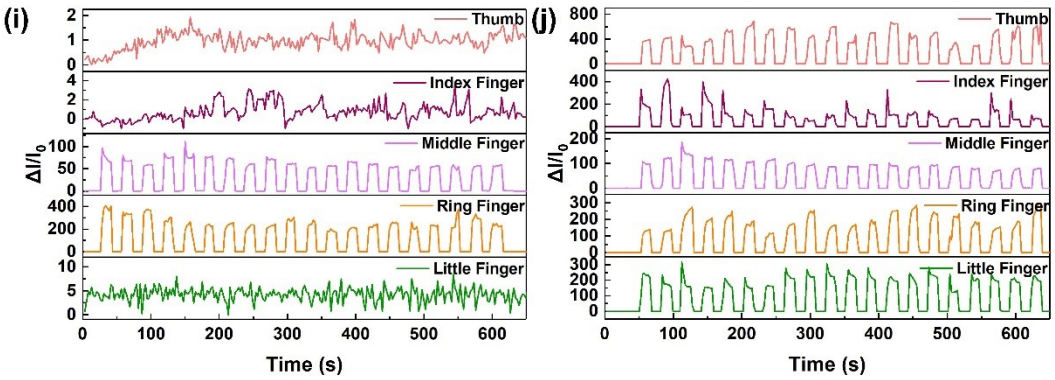

Figure S19. The current signals of ten complex gestures, (a) gesture One (thumb, middle finger, ring finger, and little finger bending), (b) gesture Two (thumb, ring finger, and little finger bending), (c) gesture Three (thumb and little finger bending), (d) gesture Four (index finger, middle finger, and ring finger bending), (e) gesture Seven (ring finger, and little finger bending), (f) gesture Eight (middle finger, ring finger, and little finger bending), (g) gesture Good (index finger, middle finger, ring finger, and little finger bending), (h) gesture OK (thumb and index finger bending), (i) gesture Rock (middle finger, and ring finger bending), (j) gesture Fist (thumb, index finger, middle finger, ring finger, and little finger bending).

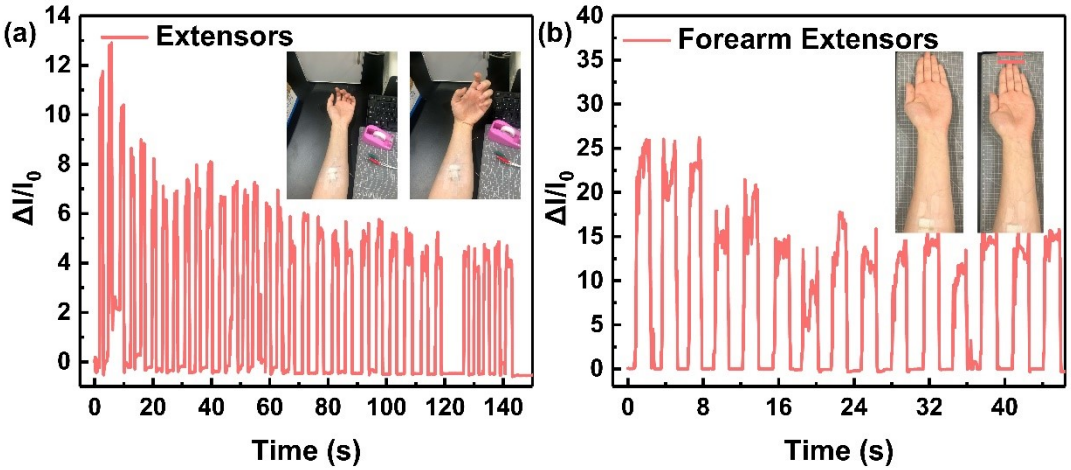

Figure S20. The monitoring of (a) extensor muscle while raising hand and (b) moving arm on table, and the different intensity of signals reflects the different degree of movement.

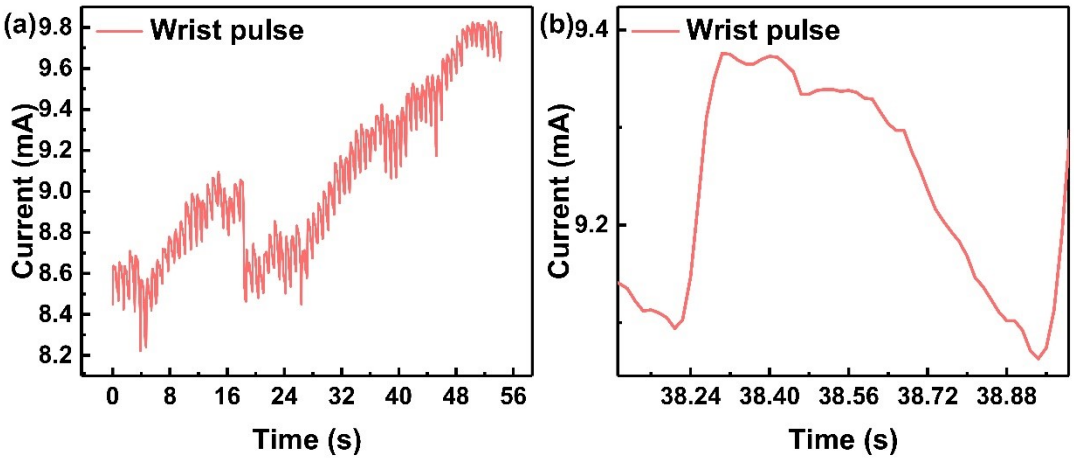

Figure S21. The recording of (a) wrist pulse and (b) one pulse signal.

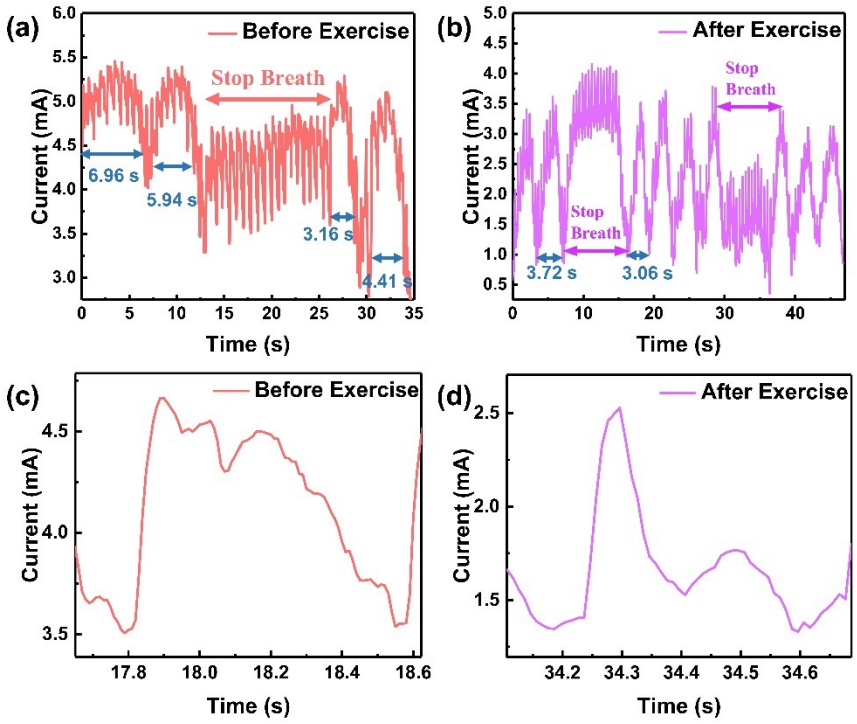

Figure S22. (a, b) The real time warning for suffocation. (c, d) One pulse signal in (a, b).

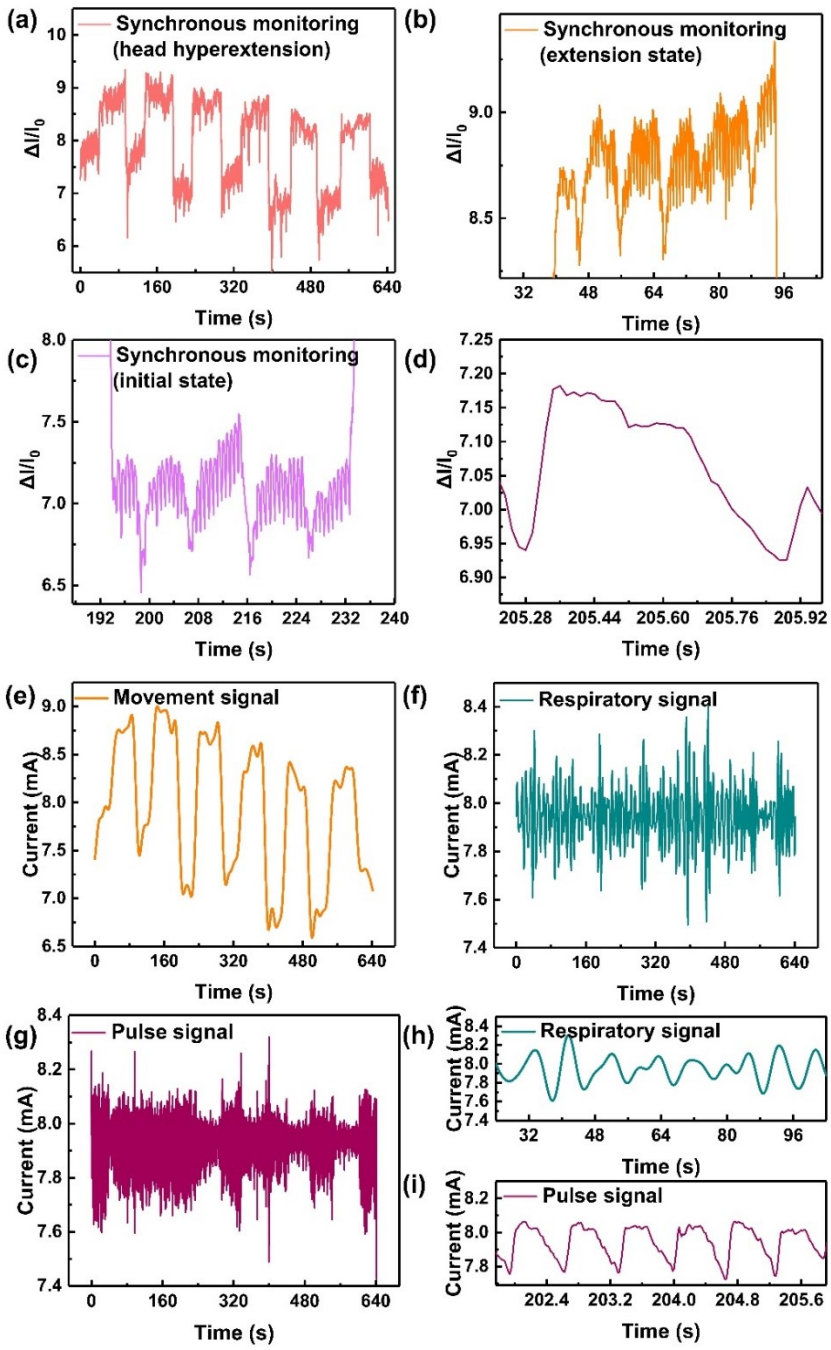

Figure S23. (a) The result of synchronous monitoring. (b) The local enlarged drawing of static raise head state. (c) The local enlarged drawing of static initial state. (d) One pulse signal in (a). (e, f, g) The movement signals, respiratory signals, and pulse signals after extracting with FFT filter. (h, i) The enlarged drawing of respiratory signals and pulse signals.

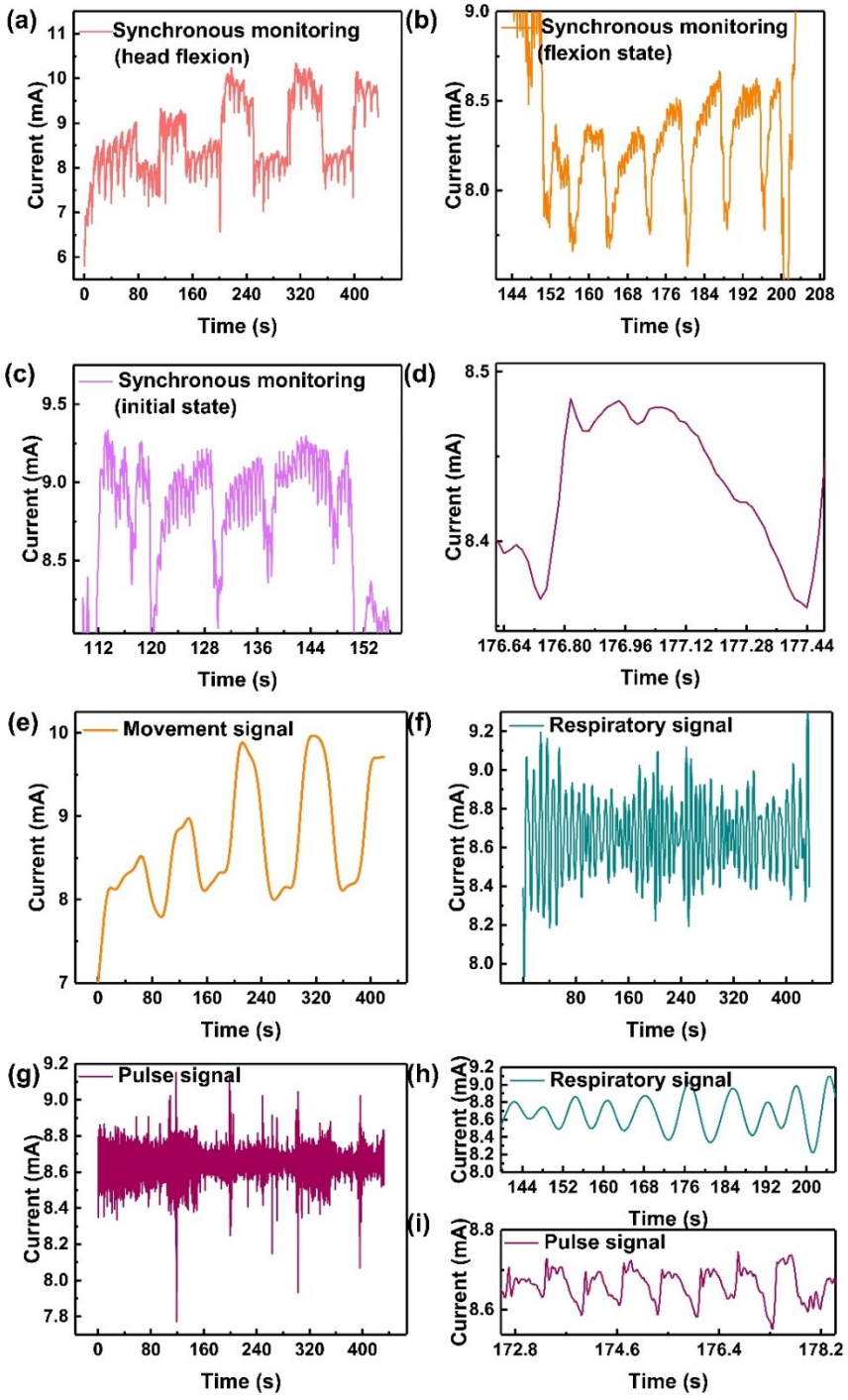

Figure S24. (a) The result of synchronous monitoring. (b) The local enlarged drawing of static bow head state. (c) The local enlarged drawing of static initial state. (d) One pulse signal in (a). (e, f, g) The movement signals, respiratory signals, and pulse signals after extracting with FFT filter. (h, i) The enlarged drawing of respiratory signals and pulse signals.

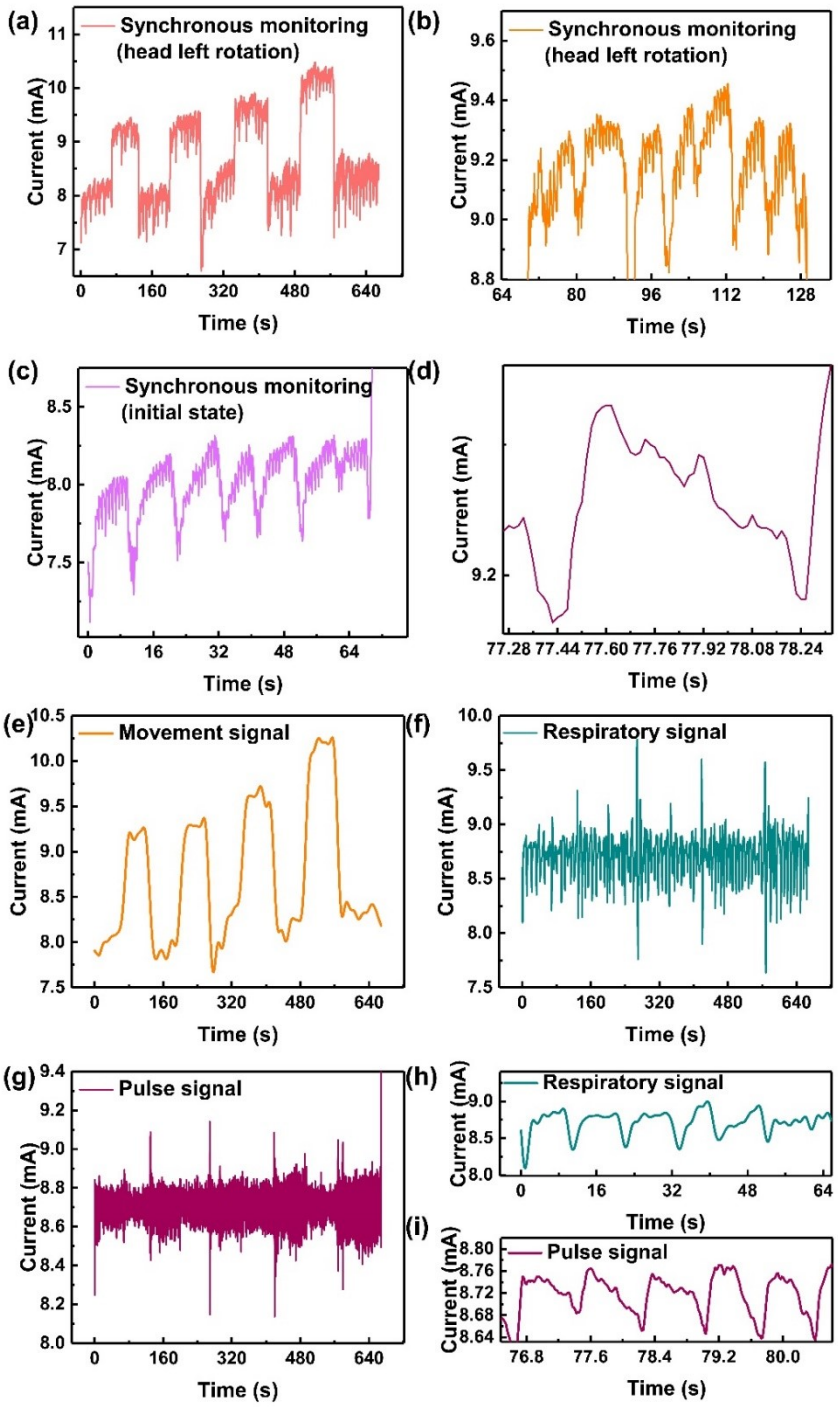

Figure S25. (a) The result of synchronous monitoring. (b) The local enlarged drawing of static turn left head state. (c) The local enlarged drawing of static initial state. (d) One pulse signal in (a). (e, f, g) The movement signals, respiratory signals, and pulse signals after extracting with FFT filter. (h, i) The enlarged drawing of respiratory signals and pulse signals.

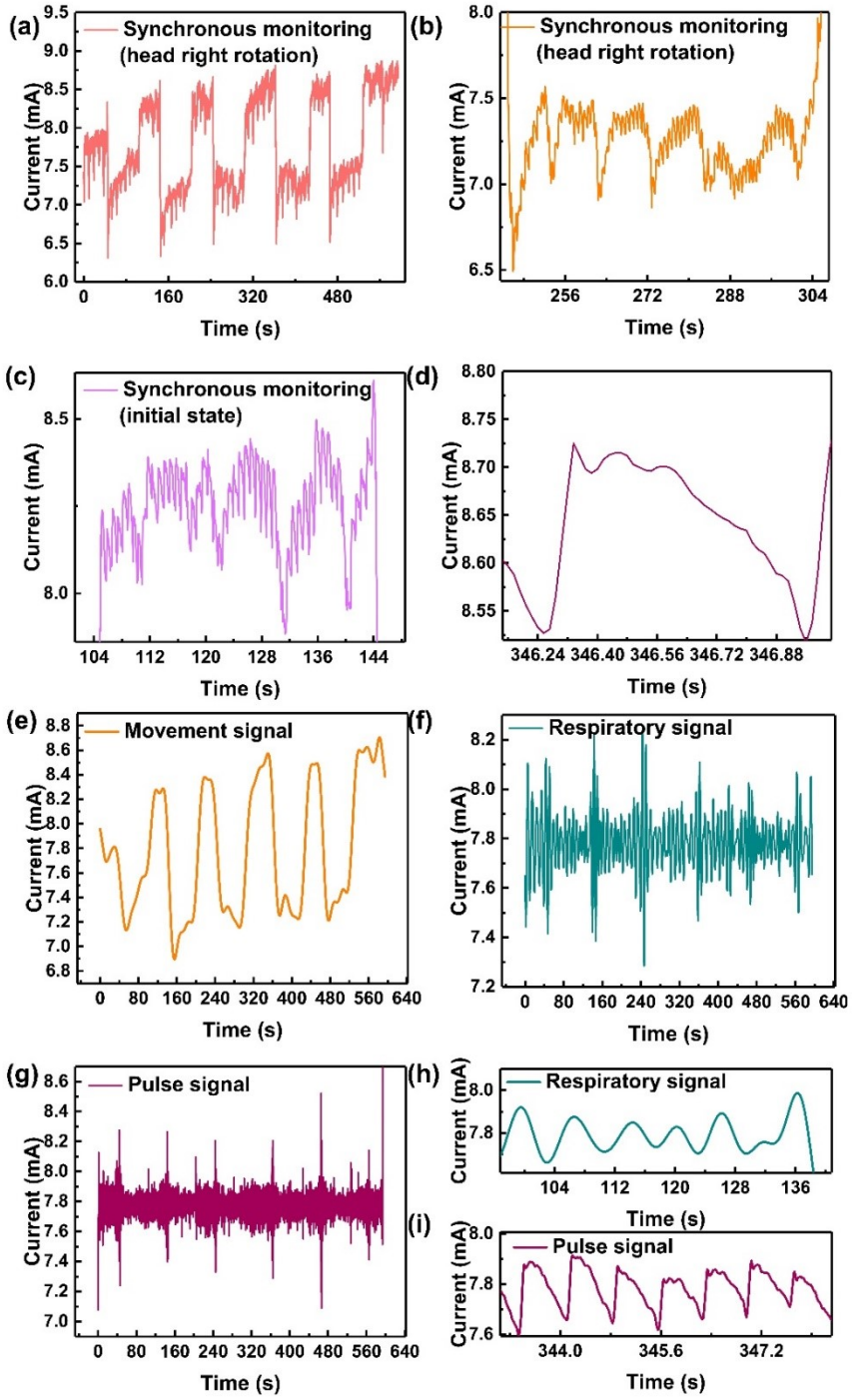

Figure S26. (a) The result of synchronous monitoring. (b) The local enlarged drawing of static turn right head state. (c) The local enlarged drawing of static initial state. (d) One pulse signal in (a). (e, f, g) The movement signals, respiratory signals, and pulse signals after extracting with FFT filter. (h, i) The enlarged drawing of respiratory signals and pulse signals.

Reference

[1] Lipatov, A.; Alhabeb, M.; Lukatskaya, M. R.; Boson, A.; Gogotsi, Y.; Sinitskii, A. *Adv. Funct. Mater*. 2016, **2**, 1600255.

[2] Hu, T.; Wang, J.; Zhang, H.; Li, Z.; Hu, M.; Wang, X. *Phys. Chem. Chem. Phys.* 2015, **17**, 9997.

[3] Ding, L.; Wei, Y.; Li, L.; Zhang, T.; Wang, H.; Xue, J.; Gogotsi, Y. *Nat. Commun.* 2018, **9**, 155.

[4] Zhang, J.; Kong, N.; Uzun, S.; Levitt, A.; Seyedin, S.; Lynch, P. A.; Qin, S.; Han, M.; Yang, W.; Liu, J.; Wang, X.; Gogotsi, Y.; Razal, J. M. *Adv. Mater.* 2020, **32**, 2001093.

[5] Ghidiu, M.; Halim, J.; Kota, S.; Bish, D.; Gogotsi, Y.; Barsoum, M. W. *Chem. Mater.* 2016, **28**, 3507.

[6] He J.; Tan B.; Su Y.; Yang S.; Wei Q. *Adv. Mater. Res.* 2012, **383**, 6293.